Non-auxetic/auxetic transitions inducing modifications of the magnetic anisotropy in CoFe2O4 thin films

E. Martin, F. Roulland, Stéphane Grenier, F. Appert, Jean Juraszek, M. Trassin, C. Bouillet, E. Chikoidze, C. Arnold, B. Berini, et al.

Non-auxetic/auxetic transitions inducing modifications of the magnetic anisotropy in $CoFe_2O_4$ thin films

E. Martin [a], F. Roulland [a], S. Grenier [b], F. Appert [c], J. Juraszek [c], M. Trassin [d], C. Bouillet [a], E. Chikoidze [e], C. Arnold [e], B. Berini [e], Y. Dumont [e], S. Colis [a], S. Barre [a], G. Versini [a], D. Preziosi [a], C. Leuvrey [a], N. Blanc [b], N. Boudet [b], G. Pourroy [a], N. Viart [a], C. Lefèvre [a]

a. Institut de Physique et Chimie des Matériaux de Strasbourg, UMR Unistra-CNRS 7504, 23 rue du Lœss, 67034 Strasbourg Cedex 2, France
b. Institut Neel, UPR 2940, F-38042 Grenoble, France
c. Normandie Univ, UNIROUEN, INSA Rouen, CNRS, GPM, 76000 Rouen, France
d. Department of Materials, ETH Zurich, Vladimir-Prelog-Weg 4, 8093 Zurich, Switzerland
e. Groupe d'Etude de la Matière Condensée (GEMaC), UMR 8635, Versailles, France

ABSTRACT

An auxetic behaviour is evidenced in $CoFe_2O_4$ thin films grown by pulsed laser deposition on (100) MgO substrates under various O_2/N_2 pressures. This rare behaviour for an intrinsic material is observed for intermediate oxidation conditions, in between two non auxetic domains delimited by high (>0.05 mbar) and low (<0.03 mbar) O_2/N_2 deposition pressures. Combining X-ray resonant diffraction and Mössbauer spectroscopy, we experimentally prove that the auxetic behaviour is related to the presence of cobalt ions in the tetrahedral sites. The impact of the structural modifications caused by the various oxidation conditions on the electronic and magnetic properties are studied for the various oxidation domains. Variations as important as a transition from a p-type semiconducting to an insulating behaviour, or from an in-plane to an out-of-plane magnetization are observed when spanning from the lowest (0.01 mbar) to the highest (1 mbar) studied oxidation pressures.

Graphical abstract

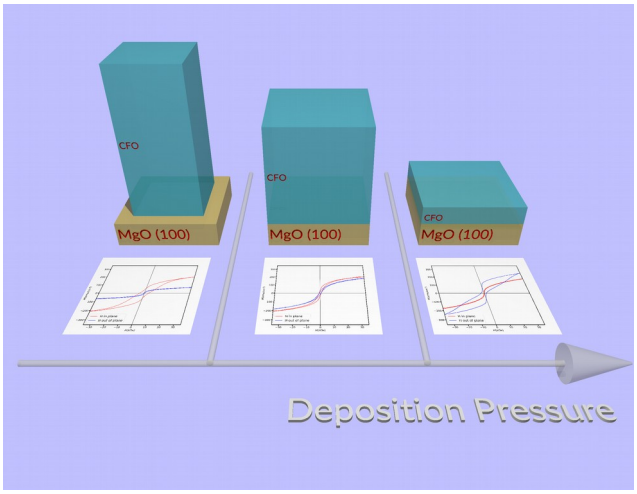

Schematic representation of both crystallographic and magnetic properties of $CoFe_2O_4$ thin films as a function of their deposition pressure

1. Introduction

Auxetics are peculiar materials that have a negative Poisson's ratio and expand (resp. shrink) under uniaxial tension (resp. compression) in the direction transverse to the load [1]. Such materials have gained considerable interest from the scientific community over the last decade thanks to their potential applications as stents [2], orthopedic bone plates [3] or skin grafts [4] in medicine, as energy absorbers in sports [5] or crashworthiness situations [6,7], as high sensitivity sensors [8,9], or as highly tunable molecular sieves [10]. The archetype of the auxetic structure is the re-entrant honeycomb network, thanks to its peculiarly designed porosity [6,11–13]. Most of the known auxetic materials are artificially designed metamaterials [14] or composites which can be patterned through 3d printing or weaving [3,15–18]. Few materials are intrinsically auxetic at the molecular level, because the structure has to feature interior empty spaces to behave in an auxetic way [19–22]. Furthermore, as shown in the recent review of R. Peng et al., 2D auxetic materials are rather rare and the huge majority are non-oxides [23]. Recently, such intriguing auxetic behaviours have been observed in perovskites [24]or spinels thin films. Hoppe *et al*. have for example observed the coexistence of enhanced saturation magnetization with an auxetic behaviour in $NiFe_2O_4$ ultrathin films [25]. Epitaxial $CoFe_2O_4$ (CFO) thin films grown on $SrTiO_3$ (STO) substrates displayed an auxetic behaviour accounted for by the hinge-like 3D honeycomb network formed by the oxygen sublattice [26]. This observation was however questioned by Foerster *et al.* who observed no auxetic behaviour, but simply an anomalously low Poisson's ratio (v) for thin films of thicknesses ranging from 4 up to 150 nm, grown on STO or on $MgAl_2O_4$ (MAO) [27]. This subject has received intensive consideration because the elastic properties are in close connection with the electronic and magnetic properties and the source of new opportunities to access to new materials properties. CFO is a well-known magnetic material involved in spintronic devices with a high Néel temperature (T_N = 793K) [28], an important saturation magnetization (Ms = 200 emu/cm^3), a large magnetic anisotropy (K = 200 kJ/m^3) [29], and good corrosion resistance and mechanical stability [30,31]. Recently, Ferreiro-Vilas *et al*. reported tuning the Poisson's ratio in CFO through the deposition method (pulsed laser deposition (PLD) *vs*. polymer assisted deposition (PAD)) [32]. While the samples grown by PLD show positive v values, samples grown by PAD have negative Poisson's ratios. The authors proposed a theoretical model stating that the auxetic behaviour of CFO is related to the distribution of Co^{2+} ions among the octahedral (O_h) and tetrahedral (T_d) sites of the spinel structure, as a result of its accommodation of the epitaxial stress.

In this paper we explore the structural, electronic and magnetic behaviours in cobalt ferrite ($CoFe_2O_4$) spinel thin films according to the O_2/N_2 deposition pressure. We bring new information concerning this compound already very studied though and show that it is possible to modulate the

mechanical behaviour of the films from auxetic to non-auxetic, the electronic properties from insulating to semiconducting, and the magnetic anisotropy form in-plane to out-of-plane, by tuning the oxidizing deposition atmosphere in a pulsed laser deposition experiment. We present here the experimental proof of the cationic redistribution in the spinel structure when the unusual auxetic behaviour is observed. While both the low and high pressure elaborated samples have a structure close to an inverse spinel, ca. ~1/4 of the tetrahedral sites are occupied by Co^{2+} for samples elaborated in the intermediate pressure range, between 0.03 and 0.05 mbar.

2. Materials and methods

2.1. Sample preparation

CFO thin films of 60 nm in thickness were elaborated by pulsed laser deposition (PLD) using a KrF excimer laser with a wavelength of 248 nm, a repetition rate of 10 Hz and an energy density on the target of 1 J/cm^2. The distance between the target and the substrate was fixed to 5 cm and the substrate temperature to 400°C. After deposition, the films were left to cool down to room temperature under the deposition pressure. The films were deposited on MgO (100) substrates (Crystal GmbH) from a ceramic CFO target in the range of [0.02 – 1] mbar of O_2:N_2. CFO (a=8.39 Å) has a cell parameter approximately double that of MgO (a=4.21 Å), and the growth is expected to be cube-on-cube with a mismatch of 0.4 %. The CFO target was synthesized using a stoichiometric mixture of Fe_2O_3 (Strem Chemicals 99.8%) and Co_3O_4 (obtained in the laboratory by calcination of cobalt carbonate $CoCO_3$, xH_2O, Aldrich). The mixture of precursors was ball milled in a teflon jar using 1 mm diameter zircon balls in an NH_3 aqueous solution. The powder was finally compacted into a 26 mm diameter pellet, and sintered in air, at 1200°C for 20 h in a platinum crucible.

2.2. Experimental methods

The Fe/Co = 2 ratio was checked by energy dispersive X-ray spectrometry (EDX). The structural (θ-2θ and reciprocal space mapping (RSM)) characterization of the thin films was carried out using a Rigaku Smart Lab diffractometer operating with a cupper rotating anode ($K_{\alpha 1}$ = 0.154056 nm). The surface and the composition of the films were studied by scanning electron microscopy (SEM) using a JEOL 6700F microscope equipped with EDX analysis. The iron to cobalt ratio in all thin films was equal to 2. Atomic force microscopy (AFM) was performed in order to have a quantitative estimate of the roughness of the sample surface. Scans of 5x5 µm^2 were performed on different locations on each sample in order to check the sample homogeneity. Lamellae of the thin films cross sections were prepared by focused ion beam (FIB) micromachining. The observations were performed using a transmission electron microscope (TEM) JEOL 2100 FCs corrected for

spherical aberration at the condenser level, with a 0.2 nn point to point resolution in TEM and 0.12 nm in scanning TEM mode (STEM). The electrical measurements were performed by using a KEITHLEY 4200-SCS semiconductor characterization system. Four electrical contacts in Ti/Au were RF sputtered on square shaped samples and two points I-V curves were recorded. A special option called “TORNADO” was developed by coupling a PPMS environment with a KEITHLEY 4200-SCS. The range of current was extended down to 10^{-10} A, the voltage up to 200 V. “TORNADO” gives the possibility to measure the resistivity, and the Hall Effect in the Van der Pauw configuration for samples with resistance up to 10^{10} Ω. Magnetic isotherm hysteresis loops were recorded at room temperature with a SQUID apparatus operating up to 7 T. DANES (Diffraction Anomalous Near Edge Structure) measurements were performed at both the Fe and Co edges (7.11 and 7.71 keV, respectively). The synchrotron experiments were carried out on the collaborating research group (CRG) D2AM beamline at the European Synchrotron Radiation Facility. Samples were mounted on a seven-circle diffractometer equipped with various photodiode detectors, allowing recording the intensity of the incident beam I_0, the intensities of the diffraction peaks and the fluorescence of the samples. The rotation matrix was preliminary determined with the help of different in-plane and out-of-plane reflections. Anomalous factors f’ and f’’ were extracted from the fluorescence data. Knowing f_0, f’ and f’’ then allows the simulation of the scans for a given set of structural parameters. The refinement of the experimental spectra was performed by minimizing the sum of all reliability factors for all reflections and edges through a stochastic basin-hopping algorithm (FitREXS program [33]). Finally, ^{57}Fe Mössbauer spectra were measured using the conversion electron Mössbauer spectroscopy technique (CEMS) on ~100% ^{57}Fe isotope enriched CFO samples. The spectra were recorded under normal incidence using a gas-flow proportional counter mounted inside a closed cycle Janis cryostat. A mixture of He-5% CH_4 gas was used at RT, whereas pure He gas was used at 80 K. The radioactive source was ^{57}Co in a Rh matrix displaced in constant acceleration mode, with an activity of about 1,8 GBq. The spectra were fitted with a least-square technique using the histogram method (MOSFIT program). Isomer shifts are given with respect to α-Fe at 300 K.

3. Results and discussion

3.1. Structural, magnetic and electrical characterizations of the CFO thin films

The oxygen-pressure-dependence of the structural properties of CFO films grown on MgO (100) were investigated by X-ray diffraction experiments. θ-2θ scans with a scattering vector parallel to the normal of the surface were used to analyse the crystalline structure of the films (Fig. 1). All scans show the expected *(002)* and *(004)* reflections of the (100)-oriented MgO substrate, as well as two other peaks corresponding to the *(004)* and *(008)* reflections of CFO. Since no other diffraction

peak is observed, we conclude to a *(00l)* oriented growth of the cobalt ferrite. (Fig. 1 and its top inset). The 2θ values corresponding to *(004)* and *(008)* CFO peaks increase when the pressure is increased, as shown in Fig. 1 for P=0.05, 0.5 and 1 mbar. Combination of both θ-2θ and RSM (reciprocal space mappings) measurements allow a complete determination of cell parameters as a function of the deposition pressure (Fig. 2). The in-plane lattice parameters were determined by RSM (Fig. 1). The zone was chosen in order to observe both the MgO *(024)* and CFO *(048)* nodes that present a four-fold symmetry. The proximity between the *(024)* node of the substrate and the *(048)* node of CFO allows an easy observation of the in-plane CFO lattice strain. The thin film and the MgO substrate display a perfect epitaxy at high pressure (Fig. 1 bottom inset), unlike the films grown at low pressure. The two in-plane cell parameters are identical for all deposition pressures and will be labeled $a_{//}$ in the following.

The variation of the out-of-plane lattice parameter, labeled $a_{\perp}$ in the following, is displayed in Fig. 2. In the [0.05-1] mbar range, it takes lower values than the bulk one as already observed in other oxides, *e.g.* $Y_3Fe_5O_{12}$ or $Ba_{0.5}Sr_{0.5}TiO_3$ [34,35]. For pressure below P=0.05 mbar (Fig. 2), the out-of-plane parameter is higher than the bulk one and increases strongly up to 8.62 Å for P=0.01 mbar. The cell parameters $a_{//}$ and $a_{\perp}$ are characterized by a monotonic but opposite evolution with pressure. The CFO unit cell undergoes a tetragonal distortion for all deposition pressures, except for the critical pressure P_c ~ 0.04 mbar, for which it is perfectly cubic. Above 0.05 mbar, the in-plane parameter $a_{//}$ is equal to 8.42 Å that is twice the lattice parameter of the substrate (a_{MgO} = 4.21 Å). The film perfectly matches onto the substrate as illustrated by the RSM in Fig. 1. The cell expands laterally due to the in-plane substrate induced tensile strain. For P ≤ 0.03 mbar, the films no longer adopt the parameters of the substrate and the ratio $a_{\perp}/a_{//}$ is greater than 1. Finally, in the intermediate pressure range [0.03-0.05 mbar], $a_{\perp}$ and $a_{//}$ are both higher than the bulk CFO lattice parameter, and despite the in-plane tensile strain of the films, the cell parameter expands in the out-of-plane direction. The variation of the films cell parameters with the deposition pressure thus allows to delimit three domains of pressures: a low pressure one, P ≤ 0.03 mbar, labelled LP in the following, an intermediate one, between 0.03 and 0.05 mbar, labelled IP and a high pressure one P ≥ 0.05 mbar, labelled HP. The Poisson's coefficient ν illustrates the unusual behaviour of IP samples. For thin films under 2D in-plane stress, *v* is expressed by:

$$v = \frac{a_{bulk} - a_{\perp}}{2a_{\parallel} - a_{\perp} - a_{bulk}}$$

where a_{bulk}=8.392 Å (JCPDS 22-1086). While both LP and HP samples show a positive *v* value, the IP sample shows a negative *v* value characteristic of an auxetic behaviour (Table 1) [27,32].

Microscopy techniques provide insights on the surface topography and on the effect of the tensile strain on the CFO thin film structure. AFM observations of the surface are shown in Fig. 3. The root mean square (RMS) surface roughness of the 0.02 mbar sample (LP) is equal to 0.1 nm indicating a low roughness related to the small mismatch between MgO and CFO. The AFM images of the HP sample display fracture lines, possibly assigned to a relaxation phenomenon along the crystallographic planes. Since this sample shows a perfect matching with the substrate, it therefore endures a 0.4% tensile strain (a_{CFO} bulk = 8.392 Å, a_{CFO} films = 8.43 Å), and some local relaxation may occur periodically through the fracture lines. HRTEM observations of cross sections have pointed out dislocations within the thin film. Red circles indicate the observed dislocations on the Fourier transform of the HRTEM observation given in Fig. 4. While both IP and HP samples show a quite similar density of dislocation, the LP thin film exhibits a value two to three times higher, that could be ascribed to the high degree of distortion of the unit cell (Table 1).

Some information on the magnetic properties of the CFO films may be determined from the room temperature hysteresis loops performed for the three pressure domains (Fig. 5). The LP samples show an in-plane easy magnetization axis, with coercive field values of about 3500 Oe and 300 Oe for the in- and out-of-plane measurements, respectively. The IP sample shows no preference for in- or out-of-plane easy magnetization direction, with comparable coercive field values for the two configurations. Finally, the HP sample exhibits an out-of-plane easy magnetization axis. The anisotropy constants, i.e. the magnetoelastic anisotropy (K_{me}) arising from the coupling between the magnetic moments and the lattice and the shape anisotropy (K_{shape}) have been calculated (see Supplementary information = SI). According to Lisfi et al [36], the contribution of the surface anisotropy (K_{surf}) is negative, since the thicknesses are lower than 300 nm. All the anisotropy constants are negative for low pressure-prepared thin films (LP), leading to negative K_{tot} value (Table 1). High pressure-prepared samples (HP) have a positive magnetoelastic anisotropy (K_{me}). Although the other contributions are negative, the total anisotropy is positive (see SI and Table 1). These results are in agreement with the in-plane and out-of-plane easy magnetization direction deduced from the magnetic hysteresis loops for LP and HP samples respectively. Finally, the magnetoelastic constant of IP sample is positive and close to zero, much smaller than the HP sample in agreement with the quasi-overlay of out-of-plane and in-plane curves.

Room-temperature I-V curves obtained for characteristic samples of the three pressure domains are displayed in Fig. 6 and the deduced resistivity is given in Table 1. The HP sample shows a very high resistance, exceeding the range of measurable resistances, $R > 10^{10}$ Ω. The thermal evolution of resistivity indicates a semi-conducting behaviour for both IP and LP samples. Extraordinary Hall

effect measurements recorded on the LP sample at 300 K and 60 kOe (not shown here) evidence positive charge carriers with concentration and mobility equal to $p = 1.3\times10^{14}$ cm^{-3} and $\mu = 5$ cm^2/Vs, respectively. Such a p-type conductivity has already been reported for spinel-type thin films and can be ascribed to the presence of vacancies in the structure [37–39].

3.2. Resonant X-ray diffraction at Fe and Co edges

Resonant X-ray diffraction was performed at both the Fe and Co edges in order to determine the cationic occupation of the tetrahedral and octahedral sites. This technique has been shown to be very sensitive to the cationic distribution [33]. Fig. 7 shows the simulated spectra for the 224 reflection of $(Co_x Fe_{1-x})[Co_{1-x} Fe_{1+x}]O_4$ as a function of the inversion parameter computed using the FitREXS software [33]. The experimental data recorded on LP, IP and HP samples at the D2AM beamline are given in the insets for both Fe and Co edges. According to the simulated spectra, one can notice that the 224 node is very sensitive to the T_d site. It is especially the case at the Co edge, for which no transition is expected in the case of purely inverse spinel structure (no Co in the T_d sites). Conversely, simulations show that the transition at the Co edge is all the more pronounced when the cobalt content increases in the T_d site. The experimental data of the three samples characteristic of the LP, IP and HP domains show a different behaviour at the Co edge. While no transition is visible for the LP sample, a small transition is observed for the HP sample and an important one is evidenced for the IP sample. The lack of transition at the Co edge for LP sample clearly indicates that the T_d site is only occupied by Fe atoms. For the two other samples, refinements of spectra recorded for different nodes of the reciprocal space, have been performed using the FitREXS software [33]. Results are shown in supplementary information and Table S1. The cobalt content of the T_d site for the HP sample (0.07) is not zero but much lower than that of the IP sample (0.24). The structures of the IP and HP samples are therefore not perfect inverse spinels, and this is even more pronounced for the IP sample. This result brings additional experimental confirmation to the model exposed by Fereiro-Vila concerning the mechanism for auxetic behaviour in CFO thin films: the auxetic behaviour appears when the degree of inversion is not complete, *i.e.* when the structure is intermediate between the direct and the inverse spinel structures [32]. The critical cationic distribution above which the auxetic behaviour appears is in the range [0.07 – 0.24].

3.3. Mössbauer spectrometry

The elongation of the CFO cell perpendicularly to the substrate observed for the low deposition pressures could have been assigned to the presence of Fe^{2+}, stemming from the reduction of Fe^{3+} under too mild oxidizing conditions. Goodenough has indeed pointed out the Jahn Teller effect that is possibly associated to Fe^{2+} [40]. The Mössbauer spectrometry is the ideal method to evidence the

valence of iron. Room temperature (RT) Mössbauer spectra of the LP and IP (as also representative of the HP samples) samples are depicted in Fig. 8 (a) and (b). All spectra exhibit a magnetic sextet with broad lines indicating a distribution of the Fe magnetic environments. They have been fitted with a distribution of hyperfine fields leading to average values of the isomer shift (δ) equal to 0.30(1) mm/s and 0.31(9) mm/s for LP and IP samples, respectively (Table 2). Those values unambiguously point out to the presence of only the high valence state of iron, Fe^{3+}. At low temperature [Fig. 8(c)], the LP spectrum is resolved enough to take into consideration two contributions of refined values of δ equal to 0.38(4) mm/s and 0.48(2) mm/s (Table 3). The refined hyperfine parameters indicate that 51,6 % of the probed iron is located in T_d site. This value is close to what observed for the bulk CFO ($Fe_{Oh}/Fe_{Td} \approx 1$) [41]. Another important feature that can be clearly seen on the RT Mössbauer spectra is the lines intensity ratio of the magnetic sextet that is different for LP and IP samples. Information about the direction of the magnetic moments can be obtained from the relative intensities of the Mössbauer absorption lines, which is given by 3:*x*:1:1:*x*:3 for pure magnetic hyperfine splitting, where $x = \frac{4\sin^2\langle\beta\rangle}{1+\cos^2\langle\beta\rangle}$ and <β> is the average "cone-angle" between the incident ɣ-ray direction and the direction of the magnetic hyperfine field. Complete in-plane spin orientation is indicated by ratios 3:4:1:1:4:3 or <β>=90°, whereas complete perpendicular orientation is present for ratios 3:0:1:1:0:3 or <β>=0°. For the LP sample, a value of <β> close to 90° is obtained from the fitting, confirming the in-plane magnetic anisotropy already deduced from the hysteresis loops measurements. A cone-angle value <β> = 48.9° is observed for the IP sample, evidencing the out-of-plane orientation of some of the Fe spins [Fig. 8(d)], in agreement with the hysteresis data.

3.4. Discussion about the chemical formula at low pressure

Assuming both cationic vacancies in the octahedral sites as encountered in maghemite (γ-Fe_2O_3) and anionic vacancies, the general formula of the CFO thin film is written

$$\left(Fe_a Co_{1-a}\right)_{Td}\left[Fe_b Co_c \boxdot_{2-b-c}\right]_{Oh} O_{4-\delta},$$

where *a* and *b* represent the iron content in tetrahedral and octahedral sites, respectively, *c* the cobalt content in octahedral sites and δ the amount of anionic vacancies per formula unit. The EDX analysis showed that Fe to Co ratio is equal to 2, *i.e.* $\frac{a+b}{1-a+c} = 2$. As shown above, the Mössbauer analysis leads to $\frac{a}{b} = \frac{51.6}{48.4} = 1.07$. The general chemical formula of the low pressure-prepared sample is thus

$$\left(Fe_{a}Co_{1-a}\right)\left[Fe_{0.94a}Co_{1.97a-1}\boxdot_{3-2.91a}\right]O_{4-\delta}$$

Taking into account the results of resonant X-ray diffraction at the Co edge of the (224) node (Fig. 7), *i.e.* the lack of transition at the Co edge for LP sample, we conclude that the T_d site is fully occupied by Fe atoms. According to Prieto *et al.* [42], the presence of some Co^{+III} within the structure can no longer be ruled out. Therefore, depending on the oxidation degree of Co atoms and taking into account the electroneutrality, the anionic vacancies content δ ranges between 0.00 and 0.24. It results in two extreme cases: 1) no Co^{+III}, which leads to δ = 0.24 : $\left(Fe^{+III}\right)\left[Fe^{+III}_{0.94}Co^{+II}_{0,97}\boxdot_{0.09}\right]O_{3.76}$, and 2) 0.24 Co^{+III}, which leads to the absence of anionic vacancies : $\left(Fe^{+III}\right)\left[Fe^{+III}_{0.94}Co^{+II}_{0.73}Co^{+III}_{0.24}\boxdot_{0.09}\right]O_{4}$. The formula for the LP sample is in the domain bounded by these extreme values. The p-type semiconductor behavior can therefore be clearly explained by the presence of cationic and anionic vacancies. The presence of Fe^{2+} being ruled out, the increase of the out-of-plane cell parameter observed for these LP samples however remains a puzzle. We are currently undertaking theoretical calculations to determine the optimal structure for CFO in the presence of such an amount of cationic (and anionic if no Co^{3+} is present) vacancies.

4. Conclusions

We have studied the influence of the oxidizing O_2:N_2 pressure on the growth of pulsed laser deposited CFO thin films on MgO(100) substrates. Increasing this pressure from 0.01 mbar up to 1 mbar, we showed that the structural, magnetic and electrical properties of CFO thin films can significantly be varied, from a p-type semiconductor behaviour with in-plane magnetization to an insulating behaviour with out-of-plane magnetization. Another important result of this study is the demonstration of the possibility to stabilize an auxetic behaviour for the intrinsic spinel CFO compound. A decrease in the O_2:N_2 oxidizing pressure is shown to induce an increase of the out-of-plane cell parameter. This increase together with the tensile stress imposed to the films by the MgO (001) substrates tend to increase the volume of the CFO cell, until the relaxation of the substrate-induced stress when the films do not adopt the parameter imposed by the substrate any more. But before that, for intermediate pressures, we could observe a situation for which the cell parameters were increased in all three directions with respect to their bulk value. In these conditions, the CFO film was shown to have a negative Poisson's ratio, *i.e.* to be auxetic. We have experimentally determined the cationic distribution in our films by resonant X ray scattering and demonstrated that, as suggested by Fereiro-Vila *et al.* [32], the auxetic behaviour was related to a high occupation of the tetrahedral sites by cobalt ions (25 %). Such a high amount of Co^{2+}_{Td} is abnormal for the spinel

structure of CFO, which should be inverse. We have even determined the limit quantity of Co^{2+}_{Td} below which CFO still adopts a non-auxetic behaviour.

An another remarkable result is the evidence of anionic and possible cationic vacancies at low pressures resulting to unexpected magnetic and electrical behaviours. The LP sample is characterized by a symmetry breaking which is not induced by the substrate. The crystal structure solution and the mechanism of distortion along the c-axis is the key point for the understanding of its properties. Theoretical developments are now in progress to better understand the involved mechanism.

Acknowledgments

This work was done with the financial support from the CNRS, the Ministère de l'Enseignement Supérieur et de la Recherche, and the laboratory of excellence Nanostructures in Interaction with their Environment (LabEx NIE 11- LABX-0058-NIE) and from Ile de France region equipment funding ("NOVATECS" C'Nano IdF Project No. IF-08-1453/R). We would like also to acknowledge support from Region of Normandy and the European Regional Development Fund of Normandy (ERDF) in the frame of the MAGMA project. We thank the IPCMS X-ray diffraction and MEB-CRO platforms.

References

[1] K.K. Saxena, R. Das, E.P. Calius, Three Decades of Auxetics Research − Materials with Negative Poisson's Ratio: A Review, Adv. Eng. Mater. 18 (2016) 1847–1870.

[2] R. Hamzehei, S. Rezaei, J. Kadkhodapour, A.P. Anaraki, A. Mahmoudi, 2D triangular anti-trichiral structures and auxetic stents with symmetric shrinkage behavior and high energy absorption, Mech. Mater. 142 (2020) 103291

[3] S. Vijayavenkataraman, A. Gopinath, W.F. Lu. (2020). A new design of 3D-printed orthopedic bone plates with auxetic structures to mitigate stress shielding and improve intra-operative bending, Bio-Des. Manuf., https://doi.org/10.1007/s42242-020-00066-8

[4] P. Mardling, A. Alderson, N. Jordan-Mahy, C.L.L. Maitre, The use of auxetic materials in tissue engineering, Biomater. Sci. 8 (2020) 2074–2083.

[5] M. Sanami, N. Ravirala, K. Alderson, A. Alderson, Auxetic Materials for Sports Applications, Procedia Eng. 72 (2014) 453–458.

[6] X. Zhang, C. An, Z. Shen, H. Wu, W. Yang, J. Bai, Dynamic crushing responses of bio-inspired re-entrant auxetic honeycombs under in-plane impact loading, Mater. Today Commun. 23 (2020) 100918.

[7] Y. Guo, J. Zhang, L. Chen, B. Du, H. Liu, L. Chen, W. Li, Y. Liu, Deformation behaviors and energy absorption of auxetic lattice cylindrical structures under axial crushing load, Aerosp. Sci. Technol. 98 (2020) 105662.

[8] B. Taherkhani, M.B. Azizkhani, J. Kadkhodapour, A.P. Anaraki, S. Rastgordani, Highly sensitive, piezoresistive, silicone/carbon fiber-based auxetic sensor for low strain values, Sens. Actuators Phys. 305 (2020) 111939.

[9] X. Rong, Y. Li, S. Han, P. Cao, Y. Zeng, W. Xu, M. Fang, W. Liu, D. Zhu, Y. Lu. (2020). Electric field modulation in the auxetic effect of BP-analog monolayer As and Sb by first-principles calculations, Phys. Chem. Chem. Phys., https://doi.org/10.1039/C9CP06933J

[10] X. Li, C. Huang, S. Hu, B. Deng, Z. Chen, W. Han, L. Chen, Negative and near-zero Poisson's ratios in 2D graphene/MoS2 and graphene/h-BN heterostructures, J. Mater. Chem. C. 8 (2020) 4021–4029.
[11] M. Mir, M.N. Ali, J. Sami, U. Ansari, Review of Mechanics and Applications of Auxetic Structures, Adv. Mater. Sci. Eng. 2014 (2014) e753496.
[12] L. Wei, X. Zhao, Q. Yu, G. Zhu, A novel star auxetic honeycomb with enhanced in-plane crushing strength, Thin-Walled Struct. 149 (2020) 106623.
[13] J.S. Hu, B.L. Wang, J.E. Li, K.F. Wang, Thermal shock resistance behavior of auxetic ceramic honeycombs with a central crack or an edge crack, Ceram. Int. 46 (2020) 11835–11845.
[14] R. Gatt, L. Mizzi, J.I. Azzopardi, K.M. Azzopardi, D. Attard, A. Casha, J. Briffa, J.N. Grima, Hierarchical Auxetic Mechanical Metamaterials, Sci. Rep. 5 (2015) 1–6.
[15] F. Agnelli, A. Constantinescu, G. Nika, Design and testing of 3D-printed micro-architectured polymer materials exhibiting a negative Poisson's ratio, Contin. Mech. Thermodyn. 32 (2020) 433-449.
[16] C. Quan, B. Han, Z. Hou, Q. Zhang, X. Tian, T.J. Lu, 3d printed continuous fiber reinforced composite auxetic honeycomb structures, Compos. Part B Eng. 187 (2020) 107858.
[17] J. Chen, Z. Du, T. Li, Structural design and characterization of highly elastic woven fabric containing helical auxetic yarns:, Text. Res. J. 90 (2019) 809-823.
[18] H. Kamrul, A. Zulifqar, H. Hu, Deformation behavior of auxetic woven fabric based on re-entrant hexagonal geometry in different tensile directions, Text. Res. J. 90 (2020) 410–421.
[19] S.C. Han, D.S. Kang, K. Kang, Two nature-mimicking auxetic materials with potential for high energy absorption, Mater. Today. 26 (2019) 30–39.
[20] A. Yeganeh-Haeri, D.J. Weidner, J.B. Parise, Elasticity of α-Cristobalite: A Silicon Dioxide with a Negative Poisson's Ratio, Science 257 (1992) 650–652.
[21] C. Huang, L. Chen, Negative Poisson's Ratio in Modern Functional Materials, Adv. Mater. 28 (2016) 8079–8096.
[22] R. Gatt, L. Mizzi, K.M. Azzopardi, J.N. Grima, A force-field based analysis of the deformation mechanism in α-cristobalite, Phys. Status Solidi B. 252 (2015) 1479–1485.
[23] R. Peng, Y. Ma, Q. Wu, B. Huang, Y. Dai, Two-dimensional materials with intrinsic auxeticity: progress and perspectives, Nanoscale 11 (2019) 11413–11428.
[24] S. Chen, C. Guan, S. Ke, X. Zeng, C. Huang, S. Hu, F. Yen, H. Huang, Y. Lu, L. Chen, Modulation of Abnormal Poisson's Ratios and Electronic Properties in Mixed-Valence Perovskite Manganite Films, ACS Appl. Mater. Interfaces 10 (2018) 18029–18035.
[25] M. Hoppe, S. Döring, M. Gorgoi, S. Cramm, M. Müller, Enhanced ferrimagnetism in auxetic $NiFe_2O_4$ in the crossover to the ultrathin-film limit, Phys. Rev. B. 91 (2015) 054418.
[26] M. Valant, A.-K. Axelsson, F. Aguesse, N.M. Alford, Molecular Auxetic Behavior of Epitaxial Co-Ferrite Spinel Thin Film, Adv. Funct. Mater. 20 (2010) 644–647.
[27] M. Foerster, M. Iliev, N. Dix, X. Martí, M. Barchuk, F. Sánchez, J. Fontcuberta, The Poisson Ratio in $CoFe_2O_4$ Spinel Thin Films, Adv. Funct. Mater. 22 (2012) 4344–4351.
[28] J. Teillet, F. Bouree, R. Krishnan, Magnetic structure of $CoFe_2O_4$, J. Magn. Magn. Mater. 123 (1993) 93–96.
[29] R. Valenzuela, Magnetic Ceramics, Cambridge University Press, 2005.
[30] P. He, K. Yang, W. Wang, F. Dong, L. Du, Y. Deng, Reduced graphene oxide-CoFe2O4 composites for supercapacitor electrode, Russ. J. Electrochem. 49 (2013) 359–364.
[31] Z. Wang, W. Jia, M. Jiang, C. Chen, Y. Li, One-step accurate synthesis of shell controllable $CoFe_2O_4$ hollow microspheres as high-performance electrode materials in supercapacitor, Nano Res. 9 (2016) 2026–2033.
[32] E. Ferreiro-Vila, L. Iglesias, I. Lucas del Pozo, N. Varela-Dominguez, C.T. Bui, B. Rivas-Murias, J.M. Vila-Fungueiriño, P. Jimenez-Cavero, C. Magen, L. Morellon, V. Pardo, F. Rivadulla, Apparent auxetic to non-auxetic crossover driven by Co^{2+} redistribution in $CoFe_2O_4$ thin films, APL Mater. 7 (2019) 031109.

[33] C. Lefevre, A. Thomasson, F. Roulland, V. Favre-Nicolin, Y. Joly, Y. Wakabayashi, G. Versini, S. Barre, C. Leuvrey, A. Demchenko, N. Boudet, N. Viart, Determination of the cationic distribution in oxidic thin films by resonant X-ray diffraction: the magnetoelectric compound $Ga_{2-x}Fe_xO_3$, J. Appl. Crystallogr. 49 (2016) 1308–1314.
[34] Y. Dumont, N. Keller, E. Popova, D.S. Schmool, M. Tessier, S. Bhattacharya, B. Stahl, R.M.C. Da Silva, M. Guyot, Tuning magnetic properties with off-stoichiometry in oxide thin films: An experiment with yttrium iron garnet as a model system, Phys. Rev. B. 76 (2007) 104413.
[35] Can Wang, B.L. Cheng, S.Y. Wang, H.B. Lu, Y.L. Zhou, Z.H. Chen, G.Z. Yang, Effects of oxygen pressure on lattice parameter, orientation, surface morphology and deposition rate of $(Ba_{0.02}Sr_{0.98})TiO_3$ thin films grown on MgO substrate by pulsed laser deposition, Thin Solid Films 485 (2005) 82–89.
[36] A. Lisfi, C.M. Williams, L.T. Nguyen, J.C. Lodder, A. Coleman, H. Corcoran, A. Johnson, P. Chang, A. Kumar, W. Morgan, Reorientation of magnetic anisotropy in epitaxial cobalt ferrite thin films, Phys. Rev. B. 76 (2007) 054405.
[37] T. Katayama, Y. Kurauchi, S. Mo, K. Gu, A. Chikamatsu, L. Galiullina, T. Hasegawa, p-Type Conductivity and Room-Temperature Ferrimagnetism in Spinel $MoFe_2O_4$ Epitaxial Thin Film, Cryst. Growth Des. 19 (2019) 902–906.
[38] A. Roy, J. Ghose, Studies on Some Titanium-Substituted Fe_2MoO_4Spinel Oxides, J. Solid State Chem. 140 (1998) 56–61.
[39] M. Seki, H. Tabata, H. Ohta, K. Inaba, S. Kobayashi, Epitaxial thin films of p-type spinel ferrite grown by pulsed laser deposition, Appl. Phys. Lett. 99 (2011) 242504.
[40] J.B. Goodenough, Jahn-Teller distortions induced by tetrahedral-site Fe^{2+} ions, J. Phys. Chem. Solids 25 (1964) 151–160.
[41] G.A. Sawatzky, F. Van Der Woude, A.H. Morrish, M\"ossbauer Study of Several Ferrimagnetic Spinels, Phys. Rev. 187 (1969) 747–757.
[42] P. Prieto, J.F. Marco, A. Serrano, M. Manso, J. de la Figuera, Highly oriented (111) CoO and Co_3O_4 thin films grown by ion beam sputtering, J. Alloys Compd. 810 (2019) 151912.

Figure captions

Fig. 1. Out-of-plane XRD pattern recorded in the 36°-46° 2θ range of $CoFe_2O_4$ (CFO) thin films elaborated at P = 0.05 mbar (blue), P = 0.5 mbar (red) and P = 1 mbar (green), respectively. Insets are (top): a magnitude around 2θ = 94°, and (bottom) the reciprocal space mapping (rsm) of the (048) node of CFO at P = 1 mbar.

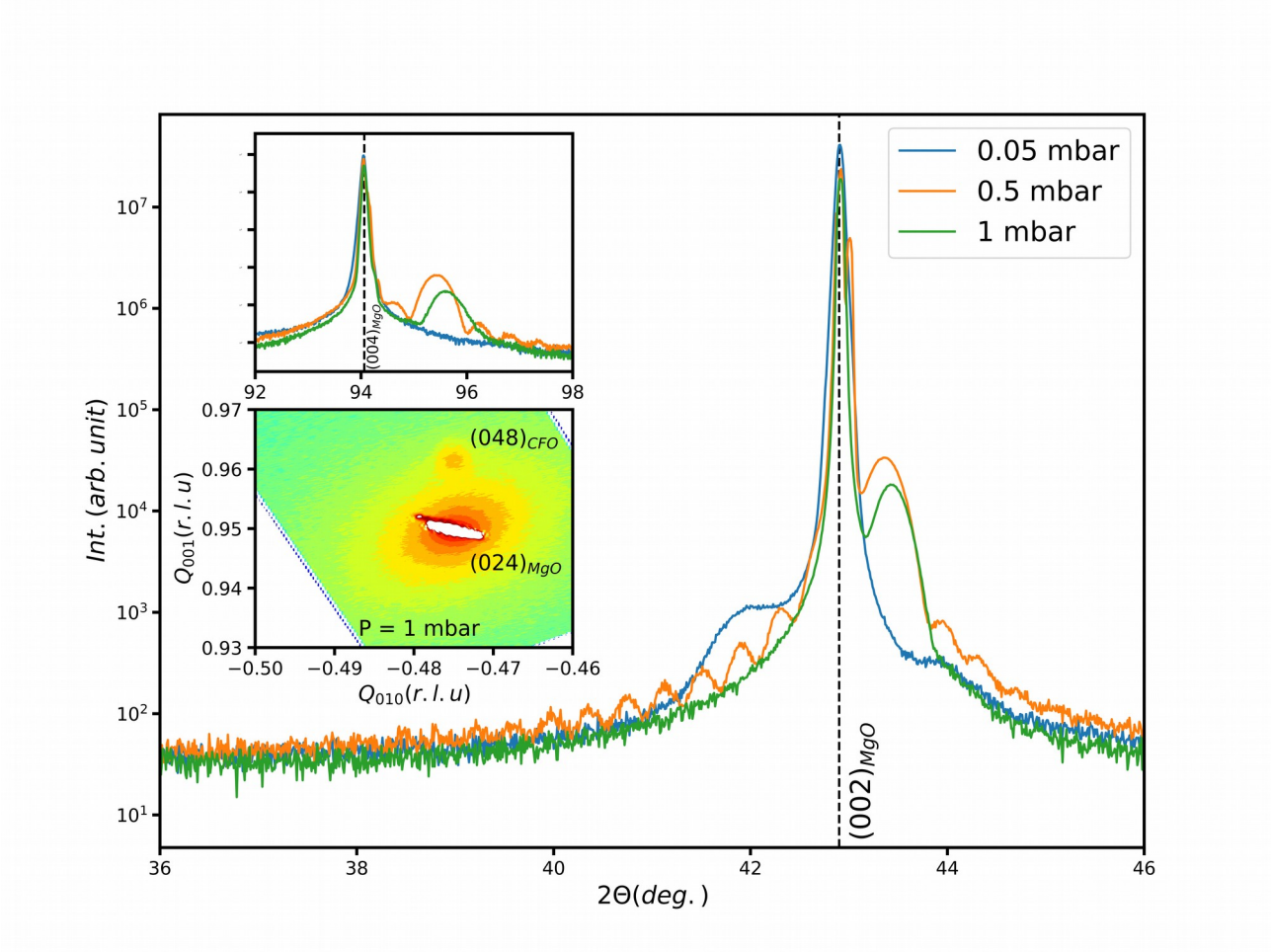

Fig. 2. Evolution of the cell parameters as a function of the pressure deposition. The dashed black line corresponds to the cell parameter of bulk cubic spinel CFO (JCPDS 22-1086). Inset shows the evolution of the volume with the partial pressure.

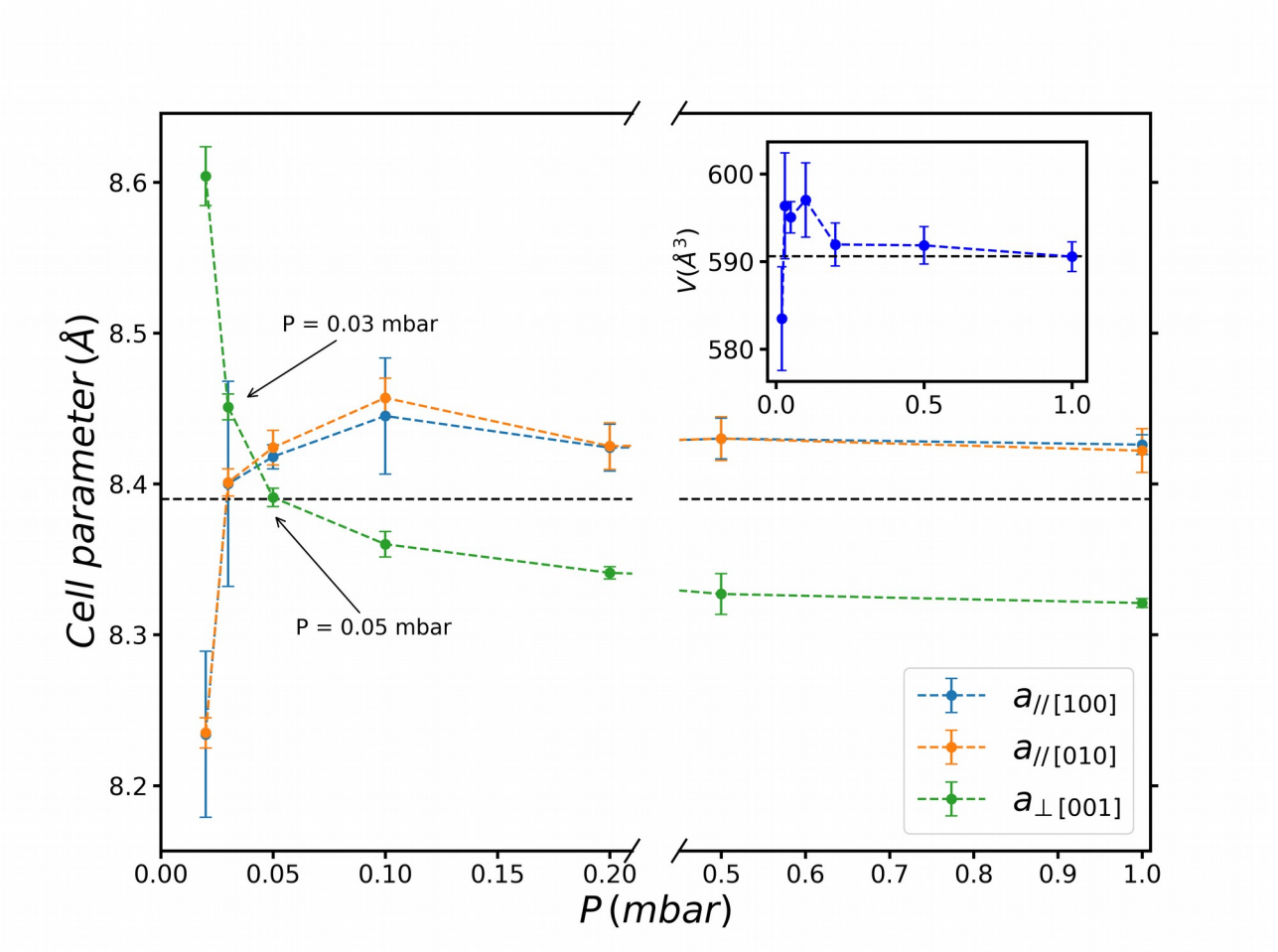

Fig. 3. AFM images of 5x5 µm² areas of $CoFe_2O_4$ thin films elaborated at P = 0.02 mbar (LP), P = 0.04 mbar (IP) and P = 0.5 mbar (HP)

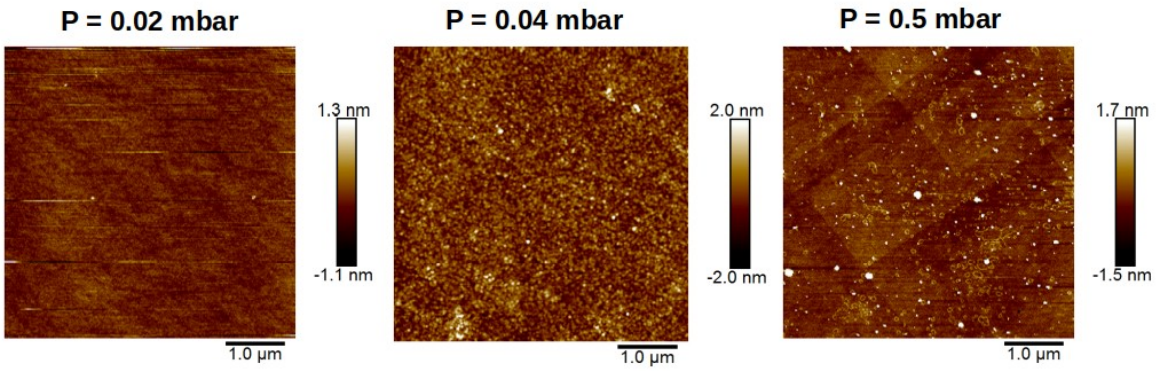

Fig. 4. TEM observations (top) and their Fourier transforms (bottom) of $CoFe_2O_4$ thin films elaborated at P = 0.02 mbar (left), P = 0.04 mbar (middle) and P = 0.5 mbar (right). Red ellipses indicate dislocations.

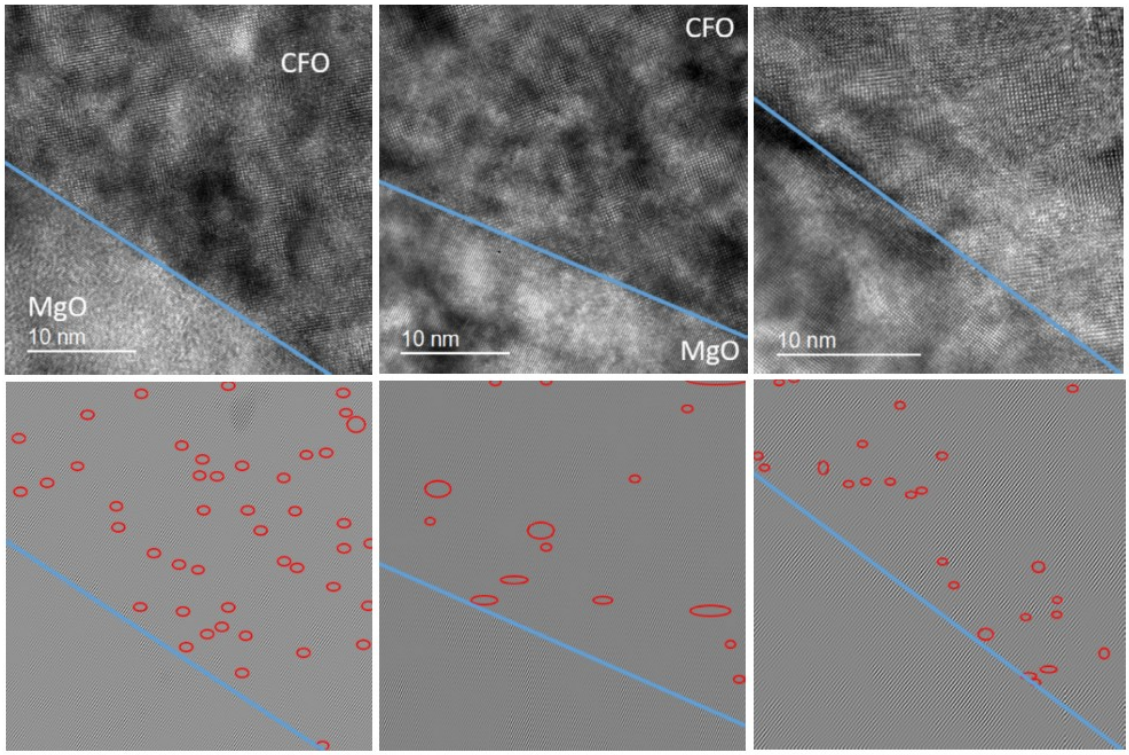

Fig. 5. Room temperature magnetic hysteresis loops measured with a maximum applied field of 70 kOe, for samples deposited at 0.02 mbar, 0.04 mbar and 0.5 mbar.

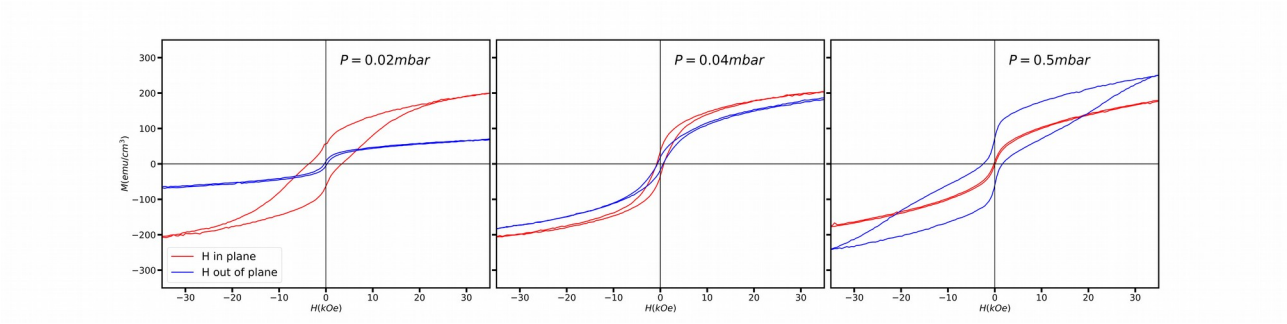

Fig. 6. Room temperature I-V curves for thin films deposited at P = 0.02, P = 0.04 and P = 0.5 mbar. The inset displays the thermal variation of resistivity.

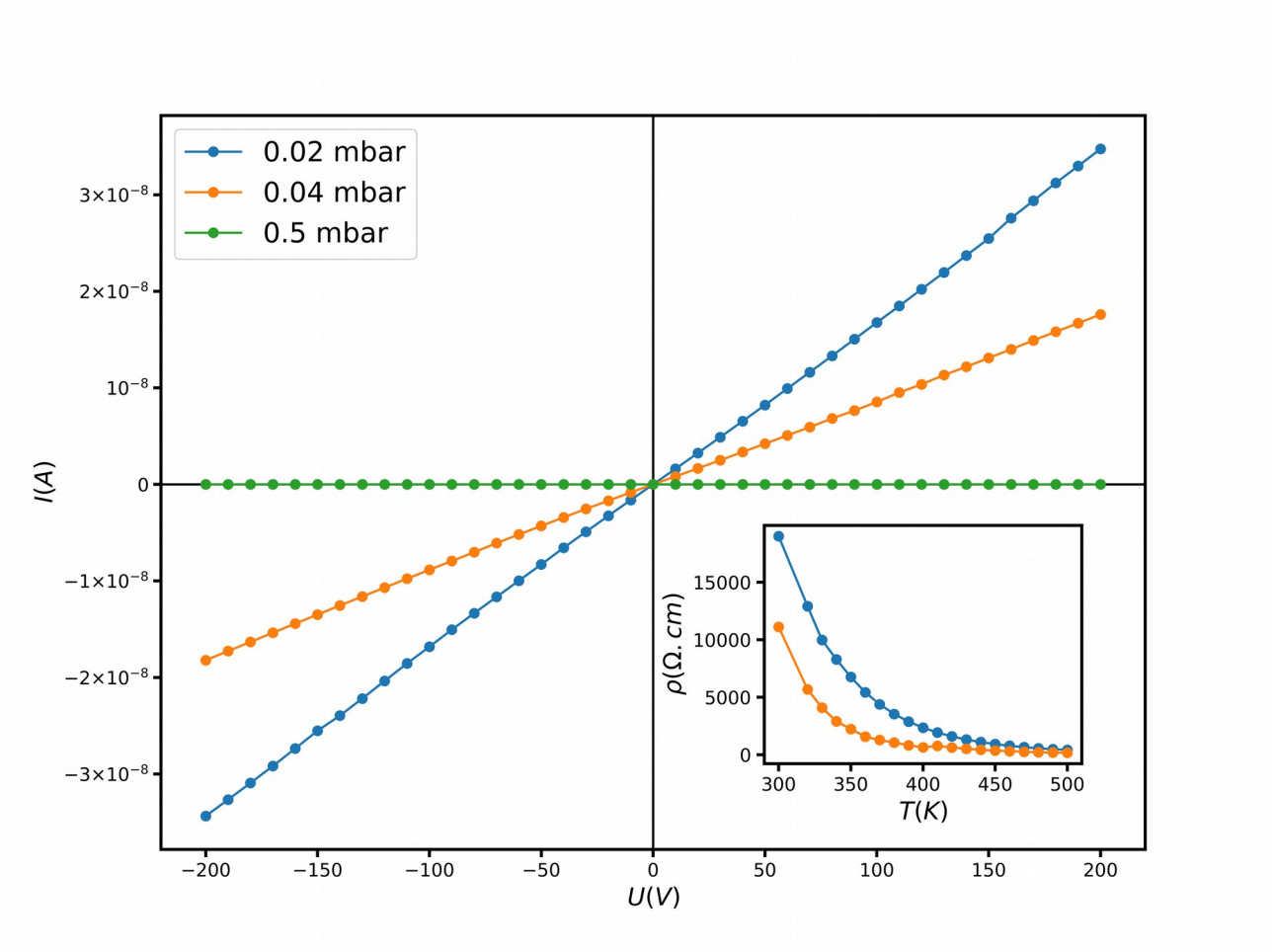

Fig. 7. Simulated resonant X-ray scattering $\left(Co_x Fe_{1-x}\right)\left[Co_{1-x} Fe_{1+x}\right]O_4$ thin films as a function of the cobalt content (x) in T_d site for the 224 node computed with the FitREXS software[21]. The experimental spectra recorded at the D2AM beamline of ESRF on low pressure (LP), intermediate (IP) and high pressure (HP) samples at both Fe and Co edges are displayed in the insets.

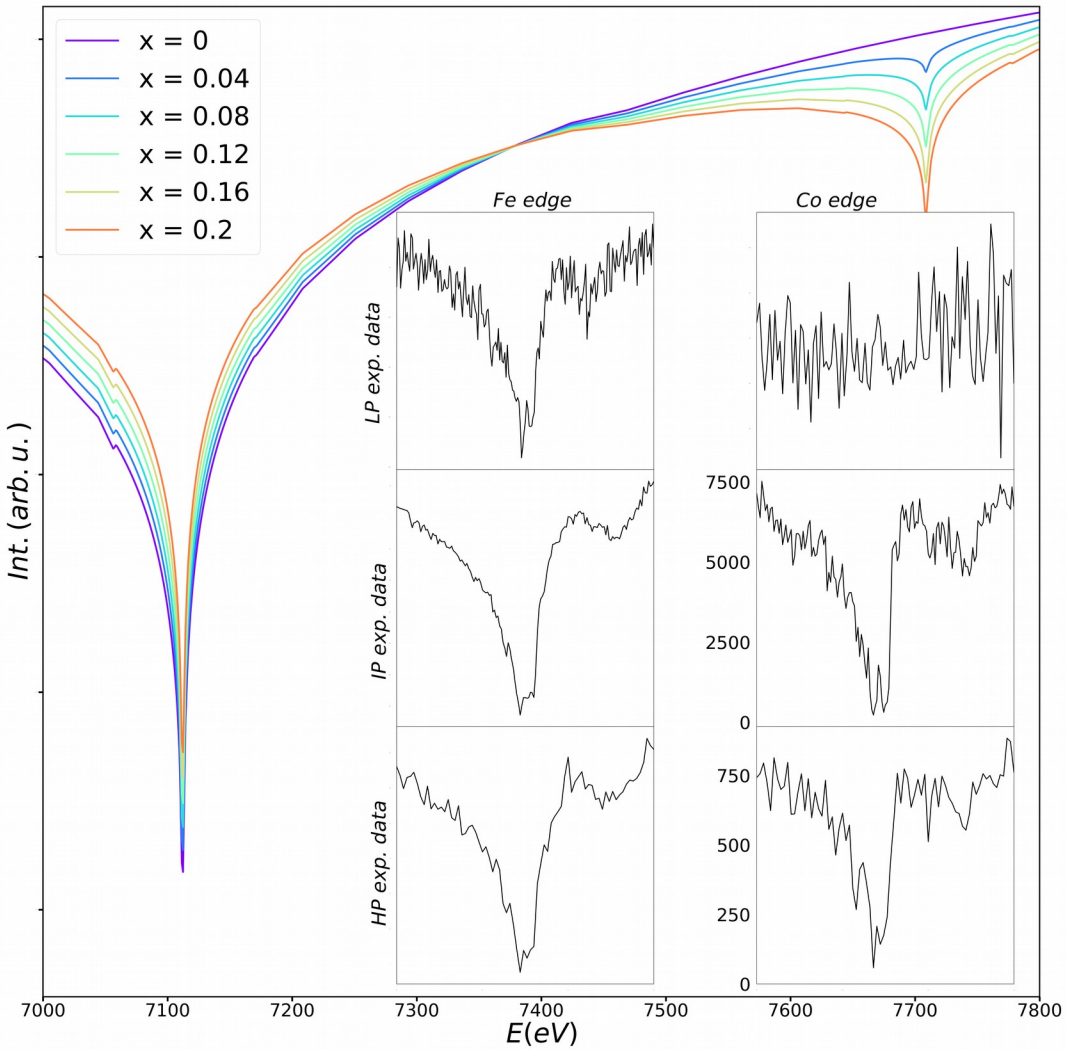

Fig. 8. (a) Room temperature Mössbauer spectra of CFO thin film deposited at P = 0.02 mbar and (b) at P = 0.04 mbar. (c) CEMS spectra at 80K of CFO thin film deposited at P = 0.02 mbar and (d) sketch of magnetic anisotropy deduced from the fit of the spectrum.

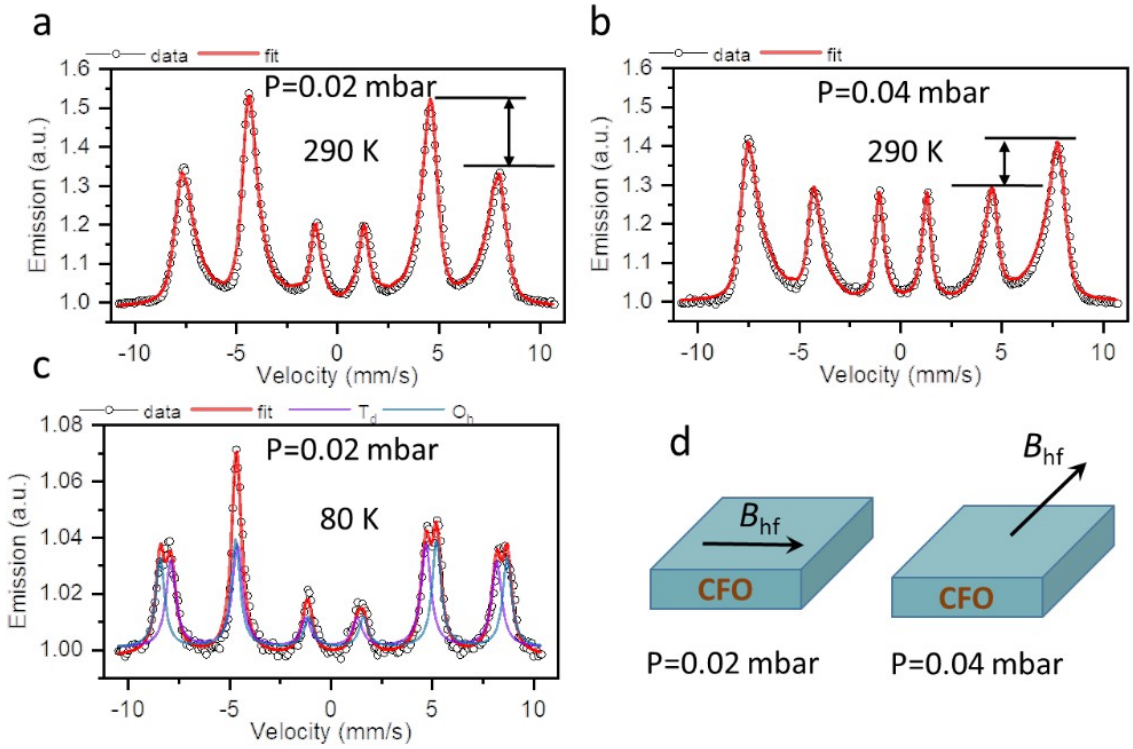

Tables

Table 1. Characteristic parameters of CFO thin films deposited at P = 0.02 mbar, P = 0.04 mbar and P = 0.5 mbar: out of plane ($a_{\perp}$) and in-plane cell parameters ($a_{//}$), ratio of the cell parameters ($a_{\perp}$ / $a_{//}$), density of dislocation deduced from TEM observation, Poisson's ratio ν, cobalt content in in tetrahedral site $(Co)_{Td}$ deduced from resonant X-ray diffraction spectra, anisotropy constants K_{tot} (see SI), resistivity at room temperature, carrier concentration and mobility.

	Low pressure (LP)	Intermediate pressure (IP)	High pressure (HP)
P(mbar)	0.02	0.04	0.5
$a_{//}$ (Å)	8.234(4)	8.446(1)	8.439(3)
$a_{\perp}$ (Å)	8.604(2)	8.419(1)	8.325(1)
$a_{\perp}$ / $a_{//}$	1.045(1)	0.997(1)	0.986(1)
number of dislocation per nm^2	0.06	0.02	0.03
Poisson's ratio ν	0.40(1)	-0.34(2)	0.42(2)
Cobalt content in tetrahedral site $(Co)_{Td}$	0.00	0.24	0.07
K_{tot} (J/m^3)	~ -59.5	~ 0	~ 15
Resistivity at 300 K (Ω.cm)	9.5×10^3	1.9×10^4	n/a
Carrier concentration	$p = 1.3 \times 10^{14}$	n/a	n/a
Mobility (cm^2/Vs)	5	n/a	n/a

Table 2. Hyperfine refined parameters deduced from the fit of the CEMS spectra at room temperature of CFO thin film deposited at P = 0.02 mbar (LP) and P = 0.04 mbar (IP).

Site	<δ> (mm.s^{-1})	<B_{hf}> (T)	<β> (°)
LP	0.30(1)	44(1)	75(2)
IP	0.31(7)	43(1)	46(2)

Table 3. Hyperfine refined parameters deduced from the fit of the CEMS spectra at 80K of CFO thin film deposited at P = 0.02 mbar (LP).

Site	<δ> (mm.s^{-1})	<B_{hf}> (T)	<β> (°)	Occupation (%)
T_d	0.38(4)	50.3(1)	72(1)	51
O_h	0.48(2)	53.6(1)	72(1)	49

Supplementary information

1. Calculation of the anisotropy constants

The total anisotropy (K_{tot}) of strained thin film can be written as the sum of the several contributions. The main one is the magnetoelastic anisotropy (K_{me}) which describes the coupling between the magnetic moments and the lattice. The other terms can be considered as correcting factors. The shape anisotropy (K_{shape}) is correlated to the demagnetizing factor which depends on the geometry of the system. Finally, the surface anisotropy (K_S) takes into account the symmetry breaking and thus deflects the moment close to the surface. The value of this last term is inversely proportional to the thickness of the samples. The total anisotropy (K_{tot}) can be thus written as:

$$K_{tot} = K_{me} + K_{shape} + \frac{2K_S}{t_c} \quad (1)$$

where t_c is the critical thickness of the film (see text).

• Due to the tetragonal distortion, the magnetoelastic constant can be formulated as [1-3]:

$$K_{me} = \frac{3}{2}\lambda_{[100]}\left(C_{11} - C_{12}\right)\left(a_{.\parallel.} - a_{.\perp.}\right)/a$$

$\lambda_{[100]}$ is the magnetoelastic constant for a distortion along the [100] direction, C_{11} and C_{12} are the elastic constants. $a_{.\parallel.}$ and $a_{.\perp.}$ are the in-plane and out-of-plane cell parameters, respectively. For this work, $\lambda_{[100]}$, C_{11} and C_{12} have been taken from Suzuki's work [4] , i.e $\lambda_{[100]} = -5.9\times10^{-4}$, $C_{11} = 2.7\times10^{12}$ dynes/cm^2, $C_{12} = 1.06\times10^{12}$ dynes/cm^2. Results of computation are given in Table S1.

• Shape anisotropy is simplified for the thin films due to the fact that $d_{33} = 1$ and 0 elsewhere in the demagnetizing tensor leading to $K_{shape} = -2\pi M^2$ where M is the magnetization [5]. Results of computation are given in Table S1.

• Lisfi *et al.* have estimated that the critical thickness t_c for CFO for the spin-reorientation transition is around 300 nm [1]. The thicknesses of our samples are smaller (~60 nm) such that the first term $2K_S/t_c$ is negative for all our samples. Since IP sample has both out-of-plane and in-plane curves which are almost superimposed, one can assume that $K_{tot} \approx 0$ involving that any external magnetic field affects the easy direction of magnetization. It results to $\frac{2K_S}{t_c} = -K_{me} - K_{shape}$ for this sample leading to $2K_s/t \sim -4.5$ J/m^3. Both LP and HP samples have same thickness as IP one. One can thus

conclude that $2K_s/t_c$ should be the same for all samples. Results of computation are given in Table S1.

Table S1

	Low pressure sample (LP)	Intermediate pressure sample (IP)	High pressure sample (HP)
K_{me} (J/m^3)	-64.2	4.7	19.7
K_{shape} (J/m^3)	-0.2	-0.2	-0.2
$2K_s/t_c$ (J/m^3)	~ -4.5	~ -4.5	~ -4.5
K_{tot} (J/m^3)	~ -59.5	~ 0	~ 15

Computation of the magnetoelastic anisotropy (K_{me}), the shape anisotropy (K_{shape}), the surface anisotropy ($2K_s/t$) and the total anisotropy (K_{tot}) of samples characteristic of the three evidenced pressure domains.

[1] A. Lisfi, C.M. Williams, L.T. Nguyen, J.C. Lodder, A. Coleman, H. Corcoran, A. Johnson, P. Chang, A. Kumar, W. Morgan, Reorientation of magnetic anisotropy in epitaxial cobalt ferrite thin films, Phys. Rev. B. 76 (2007) 054405.

[2] R. Thamankar, A. Ostroukhova, F.O. Schumann, Spin-reorientation transition in Fe_xNi_{1-x} alloy films, Phys. Rev. B. 66 (2002) 134414.

[3] B. Schulz, K. Baberschke, Crossover from in-plane to perpendicular magnetization in ultrathin Ni/Cu(001) films, Phys. Rev. B. 50 (1994) 13467–13471.

[4] Y. Suzuki, G. Hu, R.B. van Dover, R.J. Cava, Magnetic anisotropy of epitaxial cobalt ferrite thin films, J. Magn. Magn. Mater. 191 (1999) 1–8.

[5] Dubowik, Shape anisotropy of magnetic heterostructures, Phys. Rev. B. 54 (1996) 1088–1091.

2. Resonant X-ray diffraction refinement of the of both IP and HP samples at both Co and Fe edges

The synchrotron experiments were carried out on the Collaborating research group (CRG) D2AM beamline at the European Synchrotron Radiation Facility. Samples were mounted on a seven-circle diffractometer equipped with various photodiode detectors, allowing recording of the intensity of the incident beam I_0, the intensities of the diffraction peaks and the fluorescence of the samples. The rotation matrix was preliminary determined with the help of different in-plane and out-of-plane reflections.

Anomalous factors were first computed using the fluorescence data. The data are first corrected for both background and air absorption. f''(E) is then extracted by using a step function to match the Sasaki values. f'(E) is then obtained using the Kramers–Kronig transform of f''(E).

Knowing f_0, f' and f'' allows thus computation the experimental scans for a given set of structural parameters. The refinement of the different spectra was performed by minimizing the sum of all reliability factors for each nodes and edges through a stochastic basin-hopping algorithm (FitREXS program) (Figures S1 and S2).

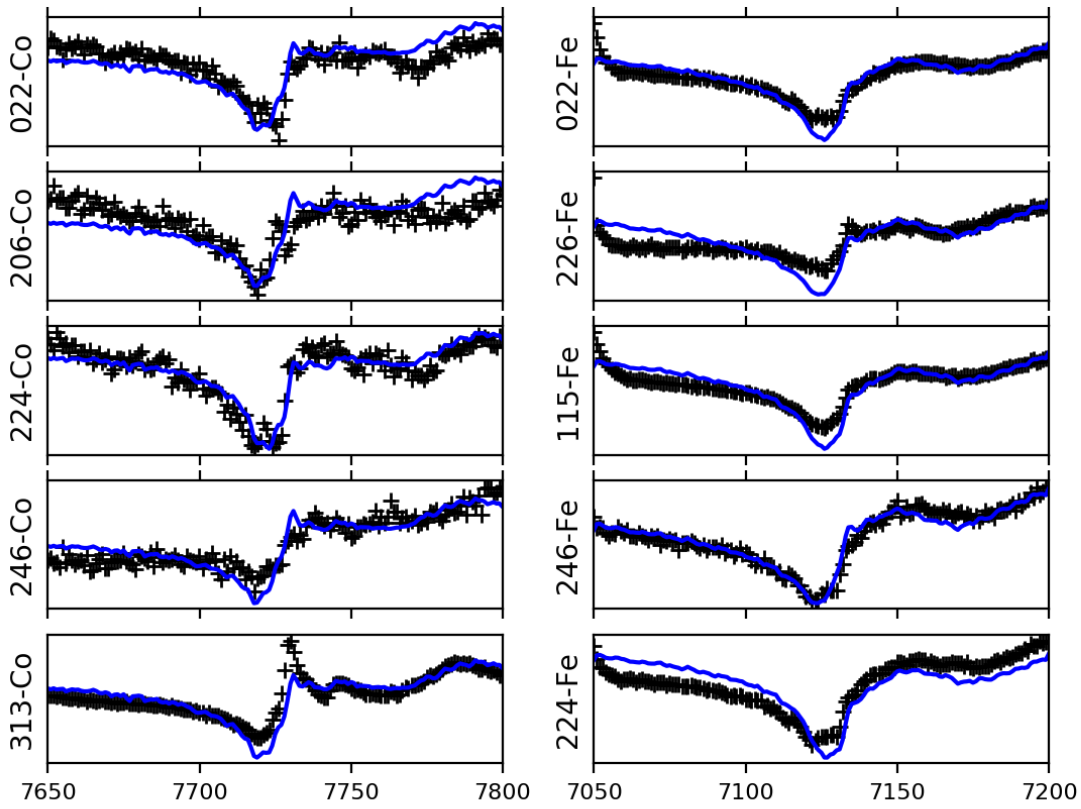

Figure S1: Refinement of IP sample at both Co (left) and Fe (right) edges. Black crosses are experimental data at different *hkl* reflections and blue curves are the refinement curves.

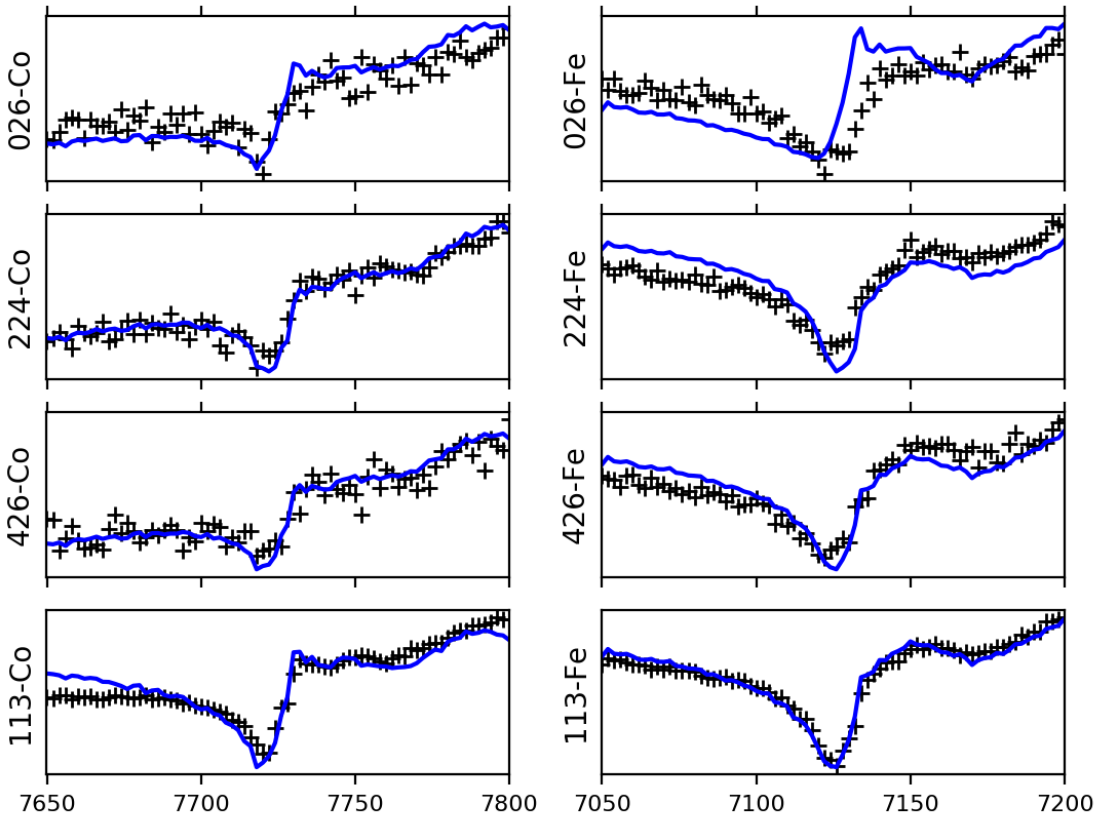

Figure S2: Refinement of HP sample at both Co (left) and Fe (right) edges. Black crosses are experimental data at different *hkl* reflections and blue curves are the refinement curves.